Bachelor Final Project

Suspension model validation for a Formula Student race car

DC2017.039

Author:
T.H.C.M. Verburg

Supervisor:
Dr. Ir. I.J.M. Besselink

University Racing Eindhoven

Eindhoven university of technology
Department of mechanical engineering
Dynamics and control group

Eindhoven, March 9th, 2017

Summary

This report describes the validation process of the suspension model for a Formula Student race car for longitudinal acceleration conditions. The emphasis lies on the validation of the installation ratio, spring and damper travel, anti-effects and static friction. Static measurements are conducted by increasing the vertical force on the rear and respectively front axle. Dynamic measurements are done by driving 75 m longitudinal acceleration runs with different axles being driven and various torque set points. The simulations are done using a MATLAB SimMechanics multi-body model.

The results from the static tests of the spring stiffness and installation ratio are inaccurate and differ from the simulation model. The static measurements can be improved by using sensors to measure the spring travel and ride height deviation, by using scales with a higher resolution and by increasing the axle mass in smaller steps. Static friction is measured to be around 2 to 3 mm on the spring travel. This corresponds to 27.5 N to 41.2 N.

The simulation results correspond closely to the measurement results for the dynamic validations. Here, the damper travel on the driven axle is in agreement with the measurements better than the damper travel for the free rolling or minor driven axle. The measured damper travels on the driven axle corresponded to the multi-body model with a deviation smaller than 1 %. The deviation on the free rolling or minor driven axle ranged from 1.2 to 7.9 %. The suspension anti-effects have a significant influence on the damper travel. In this case, the measured damper travels corresponded within 1.1 % of the multi-body model damper travels.

In the multi-body model, the center of gravity height of the sprung mass is corrected from being the center of gravity height of the entire vehicle. Furthermore, the damper travel is altered to be zero when the suspension is completely rebounded.

The estimation of the tire-road friction coefficient can be improved, since the coefficient in the rear wheel drive acceleration runs is measured to be 1.05 and for the front wheel drive acceleration runs to be 0.65. Furthermore, for the validation of the damper travel, it is uncertain what causes the deviation between the measurement results and the multi-body model results to be larger for the free rolling or minor driven axle.

Acknowledgements

I would like to thank several people who helped my during this bachelor thesis.

First of all I would like to thank Igo Besselink for his guidance and advice throughout this bachelor thesis, which kept me going. Furthermore, I would like to thank him for his ongoing support towards URE.

Secondly I would like to thank Zjelko Parfant for all his help with the multi-body model. Helping me to understand how it works and his contribution to solving the existing errors in the model, but also the mistakes I made myself. I really appreciate that he was always available and willing to help.

Thirdly, I would like to thank Robbin van Hoek for his continued support on all kinds of subjects, in- and outside the scope of this thesis.

Fourthly, I would like to thank Eveline Verburg and Elise Levert on their textual feedback on this thesis.

Finally, I would like to thank the URE team for allowing me to do this thesis with the team, the help with the track tests and the general interest in this thesis.

Nomenclature

Symbol	Description	Unit
a	longitudinal distance between front axle centre and CoG	$[m]$
A	frontal surface	$[m^2]$
a_x	longitudinal acceleration	$[m/s^2]$
a_y	lateral acceleration	$[m/s^2]$
b	longitudinal distance between rear axle centre and CoG	$[m]$
c	longitudinal distance between front axle centre and CoP	$[m]$
C_D	coefficient of drag	$[-]$
C_L	coefficient of lift	$[-]$
d	longitudinal distance between rear axle centre and CoP	$[m]$
F_D	aerodynamic drag force	$[N]$
F_L	aerodynamic lift force	$[N]$
F_s	spring force	$[N]$
F_x	longitudinal force	$[N]$
F_y	lateral force	$[N]$
F_z	vertical force	$[N]$
g	gravitational constant	$[m/s^2]$
h_{CoG}	center of gravity height	$[m]$
h_{CoP}	center of pressure height	$[m]$
h_r	vertical distance between the road and the chassis	$[m]$
i_{IR}	installation ratio	$[-]$
K_D	simplified drag coefficient	$[N/s^2]$
K_L	simplified lift coefficient	$[N/s^2]$
k_r	overall vertical suspension stiffness	$[kg/cm]$
k_s	spring stiffness	$[kg/cm]$
k_t	vertical tire stiffness	$[kg/cm]$
k_w	vertical wheel center stiffness	$[kg/cm]$
l	wheelbase	$[m]$
l_s	spring length	$[m]$
p_b	rear/front longitudinal force or torque distribution during braking	$[-]$
p_d	rear/front longitudinal force or torque distribution during driving	$[-]$
R_r	tire effective rolling radius	$[m]$
R_t	unloaded tire radius	$[m]$
T_x	driving torque	$[Nm]$
v_x	forward velocity	$[m/s]$

Greek symbols	Description	Unit
Δ	change or displacement in a variable	$[-]$
μ	tire-road friction coefficient	$[-]$
ρ	air density	$[kg/m^3]$
θ	support angle	$[degrees]$

Subscripts	**Description**
CoG	center of gravity
CoP	center of pressure
F	front
R	rear
D	aerodynamic drag
L	aerodynamic lift
FW	front wing
UT	undertray
RW	rear wing
AWD	all wheel drive
FWD	front wheel drive
RWD	rear wheel drive
FD	final drive
IR	installation ratio
IC	instant center
WC	wheel center
b	braking
d	driving or driver
v	vehicle
s	spring
t	tire
w	wheel
x	longitudinal direction according to the ISO sign convention
y	lateral direction according to the ISO sign convention
z	vertical direction according to the ISO sign convention
FL	front left corner of the vehicle
FR	front right corner of the vehicle
RL	rear left corner of the vehicle
RR	rear right corner of the vehicle
RTF	rear top front suspension bracket
$Bottom$	lowest point on the RTF bracket
$Middle$	middle point on the RTF bracket
Top	upper most point of the RTF bracket
$unsprung$	the part of the vehicle supported above the suspension
$sprung$	the part of the vehicle supported below the suspension
tot	the entire vehicle
MBM	multi-body model
FS	Formula Student

Contents

1 Introduction

University Racing Eindhoven, abbreviated as URE is a multidisciplinary student team consisting of around 50 students. They design, build, test and race with a single-seater formula race car in the Formula Student competition since 2003. Formula Student is the greatest worldwide design competition for students with events taking place all over the world. In this competition a race car is evaluated in both static and dynamic events.

In 2017, URE will compete in this competition with the URE12, the third four-wheel driven electric race car developed by the team. For the URE12, the primary focus is reliability. Therefore, the suspension of the URE12 is nearly identical to the suspension of the previous car, the URE11. Besides improving the reliability, increasing the performance of the car is always the goal. To increase the performance of the existing vehicle the control algorithms and the suspension set-up can be altered. When altering the suspension set-up there are many parameters to tune, from spring and damper characteristics to wheel alignment, tire pressure and so on. Before doing so, it first needs to be clear how all these parameters affect the vehicle behavior and more importantly, what the designed and produced suspension geometry is. Since the vehicle is hand made by students there it is most likely that there are differences between the designed and produced suspension.

In order to validate the suspension behavior, static and dynamic measurements will be conducted. In this thesis, the focus is on longitudinal acceleration. The suspension behavior is analyzed using different drive torque set-points and different axles being driven. The installation ratio, spring and damper travel, several anti-effects and the static friction in the suspension will be analyzed.

URE has build several vehicle simulation models. With these models various aspects of the vehicle behavior can be researched. These models consist of a single track, two-track and multi-body model. In the multi-body model the complete suspension is modeled, which makes it possible to analyze the kinematic behavior in detail. To see if the simulated behavior represents reality, a comparison will be made between the suspension measurements and the multi-body model.

In this thesis, first the suspension parameters are explained in a theory studyliterature review. The validation of the suspension for static conditions follows in Chapter 4 and the validation for dynamic conditions in Chapter 5. In these two chapters, first the measurements are explained and their results are analyzed. Thereafter, the results from the simulations are compared to the measurement results. In Chapter 6 some improvements to the multi-body model are explained. Finally, conclusions and recommendations are given in Chapter 7.

2 The URE11

The URE11 is the seventh electric and second four-wheel driven race car of University Racing Eindhoven. It features all self-developed carbon fiber reinforced plastics (CFRP) monocoque, in-wheel motors, accumulator, inverter, double wishbone suspension and aerodynamic package consisting of a front wing, rear wing and undertray.

2.1 Vehicle parameters

The URE11's vehicle parameters that will be used in this thesis are listed in Table 2.1. The aerodynamic parameters are obtained from a validated computational fluid dynamics (CFD) model. The other parameters are measured on the actual vehicle

Table 2.1: *The URE11's vehicle parameters*

Description	**Symbol**	**Value**	**Unit**
vehicle mass	m_v	197	kg
driver mass	m_d	75	kg
total vehicle mass with driver	m_{tot}	272	kg
wheelbase	l	1.530	m
track width front	$t_{w,F}$	1.207	m
track width rear	$t_{w,R}$	1.144	m
rear weight distribution	w_d	0.56	$-$
longitudinal distance between front axle center and CoG	a	0.86	m
longitudinal distance between rear axle center and CoG	b	0.68	m
longitudinal distance between front axle center and CoP	c	0.81	m
longitudinal distance between rear axle center and CoP	d	0.72	m
CoG height	h_{CoG}	0.30	m
CoP height	h_{CoP}	0.38	m
unloaded tyre radius	R_t	0.230	m
final drive ratio	i_{FD}	11.56	$-$
installation ratio	i_{IR}	0.717	$-$
lift coefficient full car	K_L	2.02	$\frac{Ns^2}{m^2}$
drag coefficient full car	K_D	0.67	$\frac{Ns^2}{m^2}$
lift coefficient front wing	$K_{L,FW}$	0.49	$\frac{Ns^2}{m^2}$
lift coefficient under tray	$K_{L,UT}$	0.49	$\frac{Ns^2}{m^2}$
lift coefficient rear wing	$K_{L,RW}$	1.04	$\frac{Ns^2}{m^2}$
drag coefficient front wing	$K_{D,FW}$	0.070	$\frac{Ns^2}{m^2}$
drag coefficient undertray	$K_{D,UT}$	0.123	$\frac{Ns^2}{m^2}$
drag coefficient rear wing	$K_{D,RW}$	0.347	$\frac{Ns^2}{m^2}$
support angle front axle	θ_F	2.61	$degrees$
support angle rear axle bottom RTF point	$\theta_{R,Bottom}$	10.52	$degrees$
support angle rear axle middle RTF point	$\theta_{R,Middle}$	6.19	$degrees$
support angle rear axle top RTF point	$\theta_{R,Top}$	-1.80	$degrees$

3 Literature review

In this chapter, the basics of load transfer, installation ratio, anti-effects and torque distribution are explained and substantiated with numerical equations, based on [1].

3.1 Load transfer

Load transfer is the effect of changing vertical tire forces when the vehicle accelerates or decelerates. A half car model is shown in Figure 3.1. In this case the aerodynamic forces are neglected.

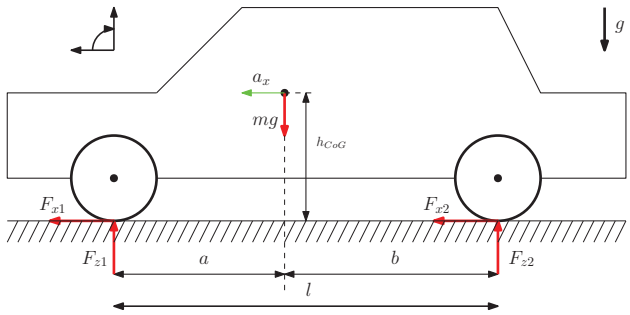

Figure 3.1: *A free body diagram of a half car model*

Using this half car model and the equations of motion that follow from it, the vertical tire forces during accelerating on the front axle $F_{z,F}$ and rear axle $F_{z,R}$ can be calculated with the following equations:

$$F_{z,F} = \frac{m_{tot} g b}{l} - \frac{m_{tot} a_x h_{CoG}}{l} \tag{3.1}$$

$$F_{z,R} = \frac{m_{tot} g a}{l} + \frac{m_{tot} a_x h_{CoG}}{l} \tag{3.2}$$

With, m_{tot} being the total vehicle mass,
g being the gravitational constant,
a_x being the longitudinal acceleration,
h_{CoG} being the center of gravity height,
a being the longitudinal distance between front axle and CoG,
b being the longitudinal distance between rear axle and CoG,
l being the wheelbase,

In these two equations, the first term equals for the static weight distribution at standstill and the second term accounts for the load transfer resulting from a longitudinal acceleration.

3.2 Aerodynamic forces

Equation (3.1) and (3.2) can be extended with the contribution of the lift- and drag force of the aerodynamic devices. These forces act at the center of pressure (CoP) and are quadratically dependent on the forward velocity v_x. Furthermore they are influenced by the air density ρ, the frontal surface A and the coefficient of lift and drag C_L and C_D. The equation for the lift- and drag force are as follows:

$$F_L = 0.5 \rho C_L v_x^2 A \tag{3.3}$$

$$F_D = 0.5 \rho C_D v_x^2 A \tag{3.4}$$

For the ease of calculating these forces, URE uses a simplified coefficient of lift and drag, K_L and K_D respectively. These are obtained from a validated computational fluid dynamics (CFD) model and are calculated as follows:

$$K_L = 0.5\rho C_L A \tag{3.5}$$

$$K_D = 0.5\rho C_D A \tag{3.6}$$

An extension of the half car model with these aerodynamic forces is shown in Figure 3.2.

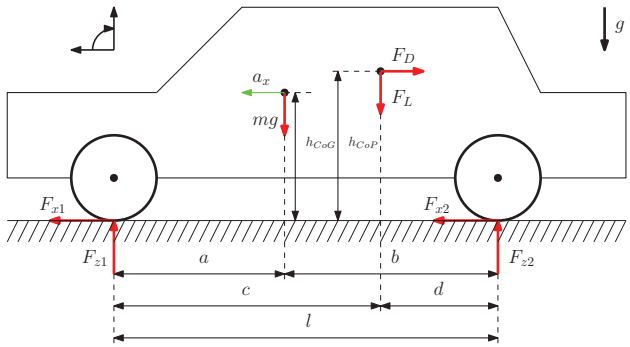

Figure 3.2: *A half car free body diagram with aerodynamic forces*

The vertical tire force equations, taking the aerodynamic forces into account become as follows:

$$F_{z,F} = \frac{mgb}{l} - \frac{ma_x h_{CoG}}{l} + \frac{F_L d}{l} - \frac{F_D h_{CoP}}{l} \tag{3.7}$$

$$F_{z,R} = \frac{mga}{l} + \frac{ma_x h_{CoG}}{l} + \frac{F_L c}{l} + \frac{F_D h_{CoP}}{l} \tag{3.8}$$

These equations show that the aerodynamic downforce F_L increases the vertical tire force on both the front and rear axle and that the drag force F_D works in the same way as the load transfer, but it is quadratic dependent on the forward velocity v_x instead of the acceleration.

3.3 Installation ratio

The installation ratio i_{IR} is the ratio between the spring displacement ΔS and the vertical wheel travel ΔW. When considering it to be constant throughout the entire suspension travel, it is defined by:

$$i_{IR} = \frac{\Delta S}{\Delta W} \tag{3.9}$$

The installation ratio is commonly confused with the motion ratio (MR), which is the inverse of the installation ratio. The installation ratio i_{IR} can be constant, meaning that ΔS increases linearly with ΔW throughout the entire suspension travel. However, the suspension geometry can also be progressive or degressive, meaning that the installation ratio increases or respectively decreases throughout suspension compression. The installation ratio is determined kinematically by the suspension design. One part of the suspension is the rocker, which is the pivot between the pushrod and the spring/damper combination, this is visualized in Figure 3.3.

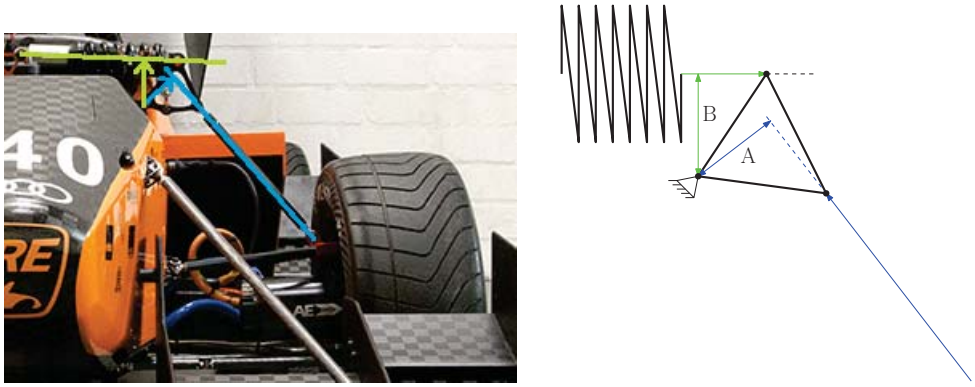

(a) The URE 11 (b) Schematic drawing

Figure 3.3: *The geometric relation which determines the ratio of the rocker, on the URE11(a) and in a schematic drawing (b)*

The installation ratio governed by the rocker (rocker ratio) is the distance from the force vector through the spring/damper combination to the rocker pivot point B (green arrow), divided by the distance from the force vector through the pushrod to the rocker pivot point A (blue arrow). This rocker ratio can be constant, meaning it will have a (near) constant value, but it can also be progressive or degressive. For a progressive suspension stiffness, the rocker ratio B divided by A will increase, for a degressive suspension stiffness vice versa. The rocker ratio can be made more degressive by, for instance, moving the damper connection point further to the left. Once this point is placed left from the pivot point, distance B will decrease under suspension compression, while distance A will still increase until a certain amount of compression.

The installation ratio determines the possible vertical wheel travel for a damper having a fixed stroke. However, it affects a few more relations. It affects the spring force F_s, dependent on the vertical tire force F_t by equation 3.10

$$F_s = \frac{F_t}{i_{IR}} \tag{3.10}$$

And it determines the vertical wheel center stiffness k_w based on the spring stiffness k_s as in equation 3.11. Whereas the spring stiffness is the force per unit displacement for a suspension spring and the wheel center stiffness is the vertical force per unit vertical displacement measured from the wheel center relative to the chassis.

$$i_{IR}^2 = \frac{k_w}{k_s} \tag{3.11}$$

Two other important stiffnesses in the suspension are the vertical tire stiffness k_t and the overall vehicle stiffness k_r. The relation between these stiffnesses and vertical wheel center stiffness is according to equation 3.12.

$$1/k_r = 1/k_w + 1/k_t \tag{3.12}$$

Figure 3.4 shows the suspension system of one corner of the vehicle. The two springs that are connected in series are k_w and k_t, the combined stiffness is equal to k_r, according to 3.12. Here, h_r is the vertical distance between the ground and the chassis. When considering the overall vehicle stiffness k_r as a spring, the ride height h_r is considered to be the corresponding spring length.

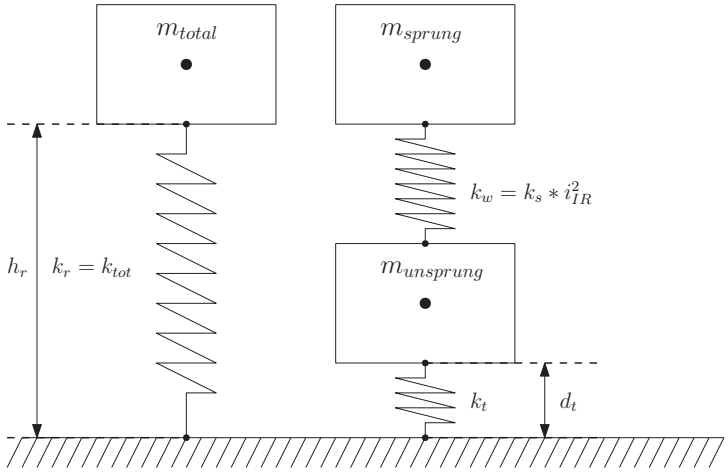

Figure 3.4: *The stiffnesses of one quarter of the suspension, left and right are equivalent*

3.4 Anti-effects

During longitudinal acceleration the vertical tire force on the rear tires increases and decreases on the front tires as shown by Equations 3.1 and 3.2. This will result in a compression of the rear suspension and an extension of the front suspension. During deceleration the opposite will happen. By introducing a support angle θ between the horizontal axis of the road surface and the line connecting the tire contact patch and the instant center (IC), the suspension compression and extension can be influenced by the longitudinal driving or braking force.
The URE11 features in-wheel motors and a double wishbone suspension. The support angle θ and the instant center are shown in Figure 3.5.

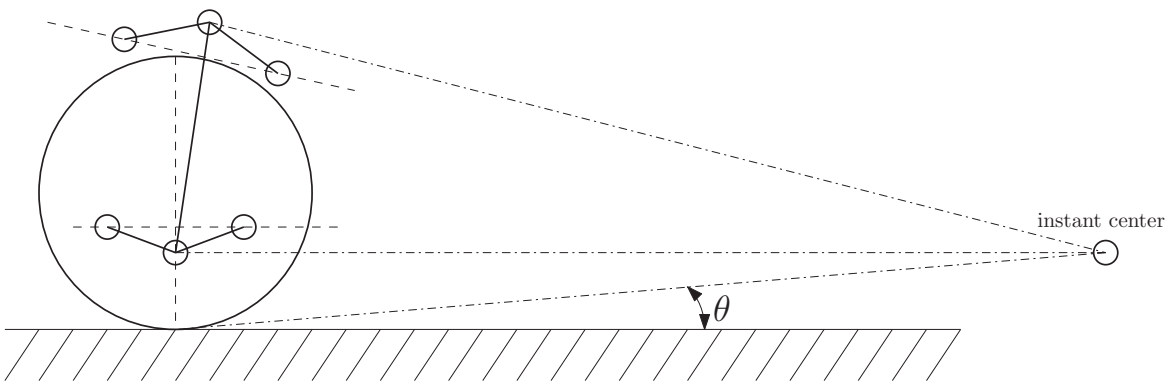

Figure 3.5: *The instant center and support angle geometry for a double wishbone suspension*

When the support angle θ is zero, the spring force, and thus spring length, is only dependent on the vertical tire force. However, when a support angle is introduced, the spring force is influenced by both the vertical tire force and the driving/braking force. A free body diagram of a rear suspension with forces applicable to longitudinal acceleration is shown in Figure 3.6.

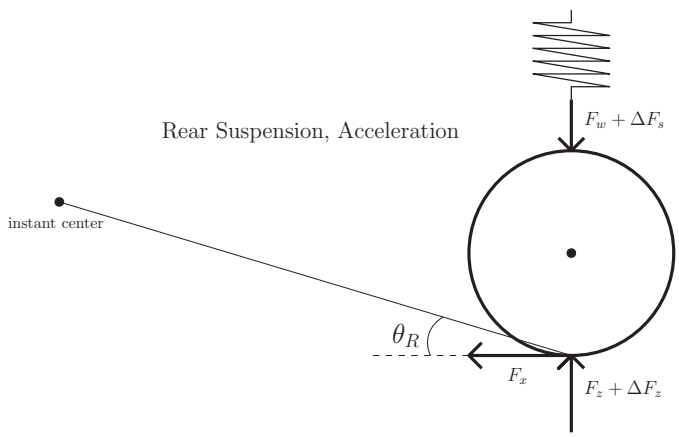

Figure 3.6: *A free body diagram of a rear suspension with a positive support angle*

The forces on the tire create a moment about the instant center. In the case of Figure 3.6, the moment of the driving force F_x counteracts the moment caused by the vertical tire force. This means that the driving force F_x reduces the spring deflection. This effect is called anti-squat, which is one of the anti-effects. In the case of a negative support angle θ the driving force F_x would increase the spring deflection the effect is then called pro-squat.

When the acceleration is zero and the longitudinal force F_x, the change of the vertical tire force ΔF_z and the change of the spring force ΔF_s are zero, we assume the vertical tire force F_z and the vertical wheel force F_w to be in equilibrium.
Looking at the rear suspension under acceleration with a support angle θ_R, the change of the spring force ΔF_s is calculated with the following equation:

$$\Delta F_z cos(\theta_R) - \Delta F_s cos(\theta_R) - F_x sin(\theta_R) = 0 \tag{3.13}$$

After rearranging this results in:

$$\Delta F_s = \Delta F_z - F_x tan(\theta_R) \tag{3.14}$$

This shows that the spring force ΔF_s, and thus spring compression, increases for an increase in vertical tire force ΔF_z, but decreases for an increase in support angle θ when a longitudinal force F_x is present. For the rear suspension under longitudinal acceleration, where ΔFz is caused by load transfer and F_x being the longitudinal force, this results in:

$$\Delta F_s = \frac{ma_x h}{l} - p_d m a_x tan(\theta_R) \tag{3.15}$$

Where p_d equals the rear/front longitudinal force distribution during driving. This is the percentage of the longitudinal force distributed to the rear axle. In case of braking, the longitudinal force F_x is affected by the rear/front longitudinal brake force distribution p_b.
The anti-effects can also be expressed as a percentage.
Front the front axle this results in:

$$anti - lift = \frac{tan(\theta_F)}{\frac{h}{(1-p_d)l}} \bullet 100\% \tag{3.16}$$

$$anti - dive = \frac{tan(\theta_F)}{\frac{h}{p_b l}} \bullet 100\% \tag{3.17}$$

For the rear axle this results in:

$$anti - squat = \frac{tan(\theta_R)}{\frac{h}{p_d l}} \bullet 100\% \tag{3.18}$$

$$anti - rise = \frac{tan(\theta_R)}{\frac{h}{(1-p_b)l}} \bullet 100\% \tag{3.19}$$

The anti-effects are dependent on the drive force distribution p_d and the brake force distribution p_b, which can be controlled by software to some extend. The center of gravity height can also change during driving, as it changes during suspension deflection. Therefore, the anti-effect percentage of a suspension is dependent on the driving situation.

3.4.1 Anti-effects on the URE11

On the URE11 the upper wishbone of the rear suspension can be tilted by adjusting the connection of the frontal top suspension attachment point. Tilting the upper wishbone changes the location of the instant center and thus the rear support angle θ_R. A picture of the rear right suspension is shown in Figure A.1 in Appendix A.

3.5 Torque distribution

For longitudinal acceleration only the front/rear torque distribution is relevant, since the vehicle is considered to be symmetric. As mentioned in section 3.1, the center of gravity position determines the static vertical tire force F_z. The load transfer and aerodynamic forces determine the change in vertical tire force ΔF_z. When load transfer results in vehicle pitch, the center of gravity position can change a bit. However, this will be neglected in the analysis.

The vertical tire force F_z, together with the tire-road friction coefficient μ, determines the maximum tire forces in the horizontal plane according to:

$$\sqrt{{F_x}^2 + {F_y}^2} \leq \mu F_z \tag{3.20}$$

Since the μ affects the maximum tire forces in the horizontal plane, it also affects the maximum possible acceleration and in turn the change of the vertical tire force ΔF_z, because of load transfer. A first estimate of the achievable longitudinal accelerations and necessary wheel torques for these accelerations can be made when not considering the wheel inertia, rolling resistance and aerodynamic drag. For a front wheel drive (FWD) vehicle, the maximum longitudinal acceleration equals:

$$a_{x,max} = \frac{\mu g b}{l + \mu h} \tag{3.21}$$

For a rear wheel drive (RWD) vehicle, the maximum acceleration is given by:

$$a_{x,max} = \frac{\mu g a}{l - \mu h} \tag{3.22}$$

And for an all wheel drive (AWD) vehicle, the maximum acceleration equals:

$$a_{x,max,AWD} = \mu g \tag{3.23}$$

For an AWD vehicle, the optimal drive torque distribution is determined as:

$$p_d = \frac{b}{l} - \frac{\mu h}{l} \tag{3.24}$$

The necessary driving torque to achieve these accelerations equals for a FWD and RWD vehicle:

$$T_x = m a_{x,max} R_r \tag{3.25}$$

For an AWD vehicle:

$$T_{x,F} = (1 - p_d) m \mu g R_r \tag{3.26}$$

$$T_{x,R} = p_d m \mu g R_r \tag{3.27}$$

With R_r being the tire effective rolling radius. For the URE11 vehicle with a driver weighing 75 kg under maximum acceleration with a μ of 1.6 this results in:
$T_{x,FWD} = 325$ Nm
$T_{x,RWD} = 791$ Nm
For an all wheel drive vehicle this results in: $p_d = 0.126$
$T_{x,AWD,F} = 122$ Nm
$T_{x,AWD,R} = 847$ Nm

However, during a longitudinal acceleration run, such as the 75 m run at a Formula Student event, the acceleration will decrease because the motor power is constant, thus the torque decreases as the wheel speed increases. With that decrease in acceleration, the load transfer decreases. Calculating the maximum wheel torque and torque distribution with a varying value for μ, gives an indication of the change in wheel torque and torque distribution for a decreasing longitudinal acceleration. When not considering the aerodynamic forces, this will result in the change in wheel torque's as shown in Figure 3.7 and the change in torque distribution as shown in Figure 3.8.

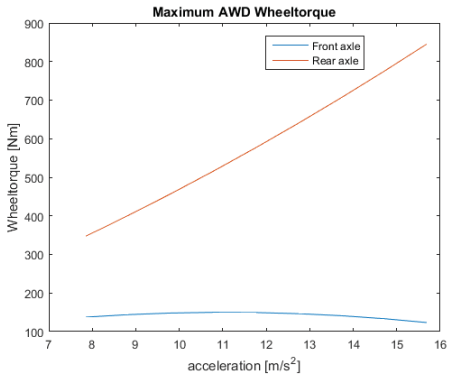

Figure 3.7: *The maximum front- and rear wheel torque as a function of longitudinal acceleration*

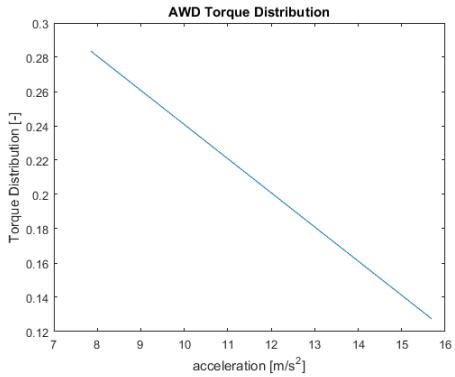

Figure 3.8: *The resulting front/rear torque distribution as a function of longitudinal acceleration*

When taking aerodynamic forces into account, the downforce F_L causes the vertical tire force on the front and rear tires to increase, with increasing forward velocity v_x. From a certain velocity, the tires will no longer be the limiting factor for the longitudinal acceleration, but the maximum amount of motor power will be. Then, there are multiple torque distributions possible, dividing a certain amount of torque over the front and rear tires, resulting in the same longitudinal acceleration.

4 Validation for static conditions

In this chapter, the suspension characteristics are evaluated for static conditions. The static friction, installation ratio i_{IR} and spring stiffnesses (k_s) are evaluated using static tests. These characteristics are also checked using the multi-body model in order to validate this model. First the static tests and the results obtained are discussed. Then, the characteristics obtained, using the multi-body model, are discussed. Finally, the results are compared and conclusions are drawn from that. Pictures of the measurement setup can be found in Appendix A. The unprocessed measurement data can be found in appendix B.

4.1 Installation ratio and spring stiffness measurement

In order to test the spring stiffness k_s and the installation ratio i_{IR}, the car is placed on leveled scales and mass, in blocks of 20 kg, is placed on the chassis near the rear and respectively front axle. The preload on the springs is set to zero. After adding the mass, the suspension is rapidly compressed and released by hand, to make sure that the suspension goes back to its equilibrium position. The installed spring stiffness equals 49 kg/cm on the front axle and 77.5 kg/cm on the rear axle. The installation ratio equals 0.717, being the damper stroke of 43 mm divided by the necessary vertical wheel travel of 60 mm. For the spring deflection, the length of the travel sensor is measured using a sliding caliper. The change in ride height, the distance between the monocoque and a beam placed on the leveled scales, is measured. This is done at three different points on one line over the width of the monocoque using a sliding caliper on the rear and a tape measure on the front. The average of these three measurements is the used value for the calculations. The added mass per corner of the vehicle is measured with the scales. These display the mass in steps of 0.5 kg.
As stated by Equation (3.9), the installation ratio can be calculated by dividing the spring travel by the vertical wheel travel. In this case the vertical wheel travel is the change in ride height minus the tire deflection. The tire pressure isn't measured in this measurement, so a pressure of 1.0 bar is assumed. As stated in Equation (3.11), the spring stiffness k_s can be calculated by dividing the vertical wheel center stiffness k_w by the installation ratio squared. The wheel center stiffness k_w is calculated using Equation (3.12). The overall vehicle stiffness k_r is the added mass on one wheel divided by the total axle change in ride height. The results of the calculated installation ratio on the rear axle is shown in Figure 4.1. The results for the measured spring stiffness using the measured value of the installation ratio $k_{s,..}$ and using the designed value of the installation ratio $k_{s,..,IR}$, on the rear axle, are shown in Figure 4.2. Here, RL stands for the rear left corner and RR for the rear right corner of the vehicle. The results for the front axle measurement are presented in Figure 4.3 and 4.4. Here, FL stand for the front left corner and FR for the front right corner of the vehicle. The installation ratio should be near constant with a value around 0.717 and the spring stiffness on the rear axle should have a constant value of 77.5 kg/cm and on the front axle of 49 kg/cm.

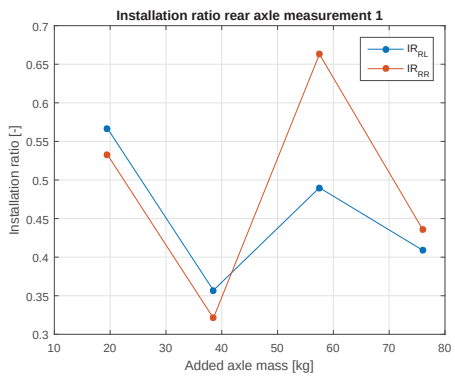

Figure 4.1: *The calculated installation ratio of the rear axle*

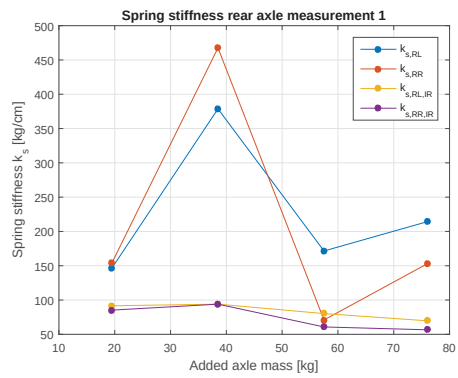

Figure 4.2: *The measurement results of the spring stiffness on the rear axle*

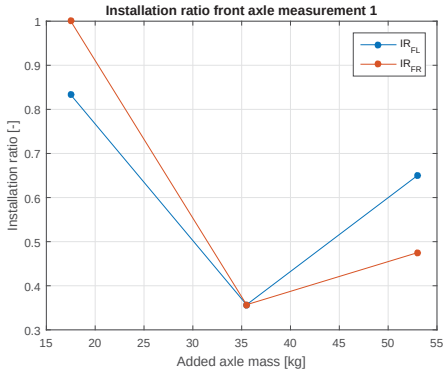

Figure 4.3: *The calculated installation ratio of the front axle*

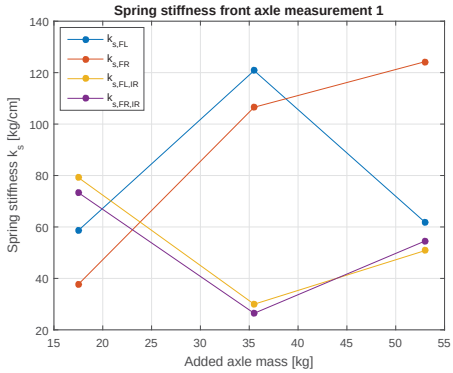

Figure 4.4: *The measurement results of the spring stiffness on the front axle*

As the installation ratio i_{IR} and spring stiffnesses k_s should be almost constant, the results show however a lot of deviation. Therefore it can be concluded that the measurement is most likely inaccurate. In order to obtain more realistic results, the measurement process needs to be improved. Measuring by hand, static friction and measuring with an unknown tire pressure are some of the possible causes for the inaccuracies seen.

4.2 Improved measurement

The accuracy of the measurement of the spring length directly influences the accuracy of the resulting spring stiffness k_s. To improve the accuracy, springs with a lower stiffness are installed on the vehicle. Lowering the stiffness from 49 and 77.5 kg/cm to 28 kg/cm on both the front and rear axle results in increased spring travel for the same change of mass on the axle. This causes a decrease in influence of the measurement error of the spring length and of the effect of friction on the measurement results. This time, the spring length is not measured on the travel sensor, but the actual spring length is measured, using a sliding caliper. This is easier to measure. By using lower spring stiffnesses, the measured change in ride height will increase. Together with an increase in spring travel, this improves the accuracy of the installation ratio i_{IR} measurement. Furthermore, in the first measurements the suspension was only rapidly compressed and released after adding mass to the axle. To know more about the magnitude of the static friction in the suspension and its influence on this measurement the suspension is now also slowly compressed and released and rebounded and released by hand. This way, measurements are done to identify the upper and lower end of the static friction region. In the first measurement, the tire pressure was not measured, so the vertical tire stiffness was uncertain. For the second measurement, the tire pressure is set precisely to 1.0 bar. The vertical tire stiffness on this pressure is classified information.
The results for the rear axle measurement are shown below. Here, RL stands for the rear left corner and RR for the rear right corner. The measured installation ratio under compression and rebound is shown in Figure 4.5. Figure 4.7 shows the results for the measured spring stiffness using the calculated installation ratio ($k_{s,..}$) and the design value of the installation ratio ($k_{s,..,IR}$), under compression. In this figure, error bars are included which represent the error margin caused by the resolution of the scales. This is explained later in this section. Figure 4.8 shows the results under the rebound condition.
The results for the front axle measurement are presented in Figure 4.6, 4.9 and 4.10. The error bars in Figure 4.9 represent the error margin caused by the resolution of the scales. The installation ratio should be near constant with a value around 0.717 and the spring stiffnesses should have a constant value of 28 kg/cm.

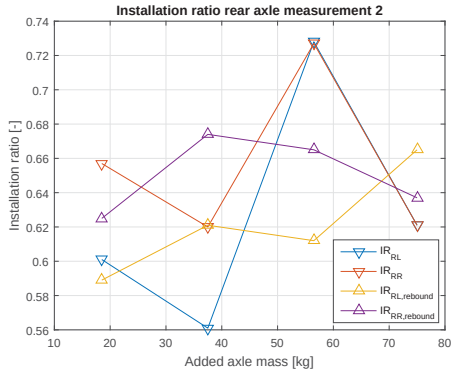

Figure 4.5: *The measurement results of the installation ratio on the rear axle*

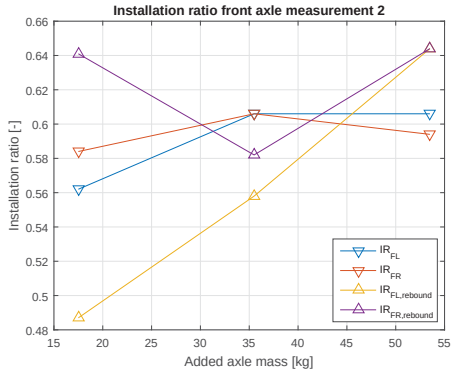

Figure 4.6: *The measurement results of the installation ratio on the front axle*

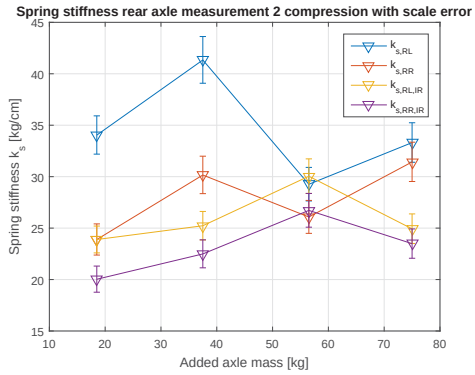

Figure 4.7: *Rear axle spring stiffness results with error bar*

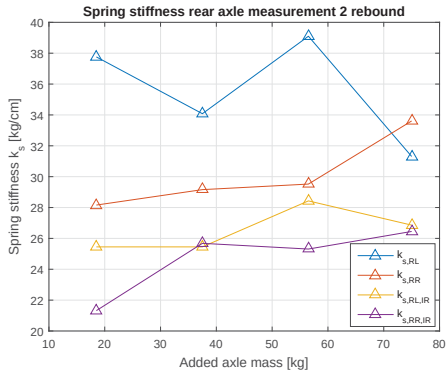

Figure 4.8: *The measurement results of the spring stiffness on the rear axle*

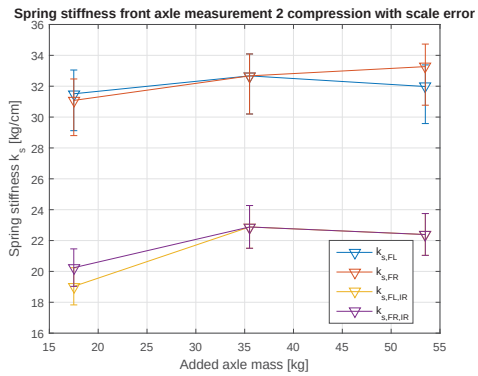

Figure 4.9: *Front axle spring stiffness results with error bar*

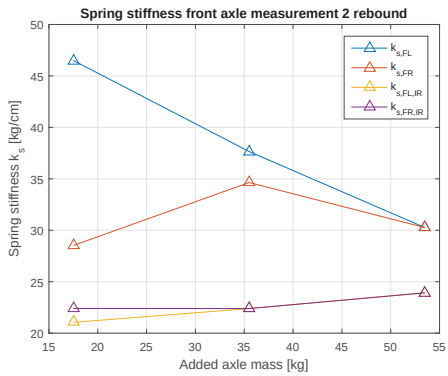

Figure 4.10: *The measurement results of the spring stiffness on the front axle*

While the results of this measurement are more consistent and closer to the design value of 0.717 and 28 kg/cm, there are still large deviations. Furthermore, there are large deviations in the spring stiffness results for using the design and calculated installation ratio. The latter are influenced by measurement errors twice. The average measured installation ratio has a value of around 0.58-0.64, which is lower than the design value of 0.717. This would mean that there is less spring travel relative to the vertical wheel travel than designed. If this is true, this could result in the URE vehicle bottoming earlier under driving and having to drive with a higher ride height or with stiffer springs.

The difference in installation ratio on the front axle could be caused by measurement errors in the change of the ride height, being measured with a tape-measure. For both the axles, a cause for the deviation in comparison to the design value could be the backlash in the suspension system or differences in the manufactured suspension.
For the spring stiffness, the deviation between measurement points could be caused by the step size of the scales. Since the scales display in steps of 0.5 kg, the error in the change of mass has a maximum deviation of 0.5 kg and a range of 1 kg. The effect of this discretisation error in the weight measurement on the results for the spring stiffness, during compression is presented in Figure 4.9 and 4.7. This is similar for the rebound case.
For the spring stiffness of the front left corner of the car, using the design value of the installation ratio, the results are presented in Table 4.1.

Table 4.1: *Front left corner spring stiffness using designed installation ratio deviation caused by the scale error*

Data point	Measured value $k_{s,FL,IR}$	Lower limit	Deviation	Upper limit	Deviation
1	20.24 kg/cm	19.03 kg/cm	6 %	21.46 kg/cm	6 %
2	22.88 kg/cm	21.50 kg/cm	6 %	24.27 kg/cm	6 %
3	22.39 kg/cm	21.04 kg/cm	6 %	23.75 kg/cm	6 %

This shows that the error in the scales causes a deviation of around 6 % up- and downwards of the measured values.

4.3 Static friction

The static friction is one of the causes for the differences between the measurement and design. The static friction causes deviation in the spring length for a certain load. For the measurement results presented previously, the spring stiffnesses are calculated after compression or rebound. The total spring travel, for multiple axle loadings, isn't considered, but only the travel for each additional loading. Therefore, the graphs do not show the effect of static friction.
The static friction in a suspension originates from the ball bearings, cylindrical bearings and the dampers. It is key to keep the bearings greased and to renew them once in a while to minimize not only the static friction, but also the backlash in the suspension. The friction in the dampers originates from the seals in the damper and from a bending moment on the piston, pushing the piston against the inner wall of the cylinder. At the end of the springs, where the winding is flattened, the stiffness is higher than in the rest of the spring. When compressing these springs, this causes the bending moment. The static friction in the suspension is measured by compressing and releasing and rebounding and releasing the suspension under every measured axle loading, measuring the spring lengths and looking at the difference between the two cases. This is shown in Figure 4.11 and 4.12.

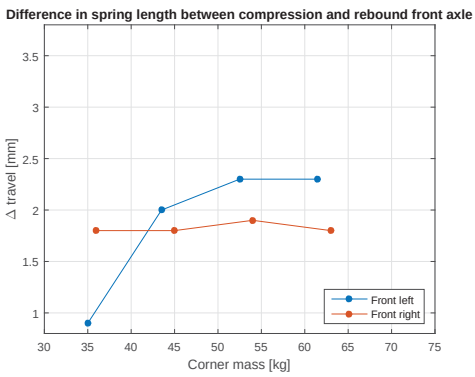

Figure 4.11: *The amount of static friction against the added axle mass on the front axle*

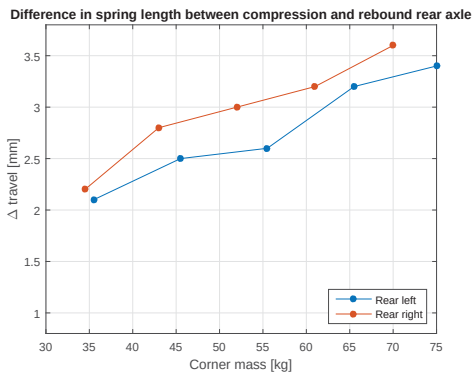

Figure 4.12: *The amount of static friction against the added axle mass on the rear axle*

The results show different levels of static friction for increased suspension loading. A linearly increasing behavior can be explained by the friction in the dampers caused by the bending moment from the springs. This bending moment is caused by the stiffness of the spring not being uniform. Therefore, the friction force increases for an increased spring travel, and thus an increase of axle mass. The static friction can be assumed to be the difference between the compression and rebound spring length divided by two. Thus, the spring spring length without static friction should be the mean of the compression and rebound case. This will give a better representation of the spring stiffness that the presented results, which only show the stiffness for the rebound or the compression case. The static friction affects the spring stiffness measurement as for a certain vertical force on the suspension, the spring length and ride height varies between the upper and lower bound of the static friction. The static friction on the front axle is around 2 mm. As this is the difference between the rebound and compression case, the spring stiffness can be assumed to be 1 mm in either direction. For a spring stiffness of 28 kg/cm this results in a friction force of 27.5 N. On the rear axle this is average 3 mm, resulting in a friction force of 41.2 N. This shows that there is a considerable amount of static friction force in the suspension. With a significant difference between the front and the rear axle.

4.4 Comparison with theoretical models

When taking a deeper look into the design installation ratio, and calculating it using the multi-body model created by Zjelko Parfant, the installation ratio shows not to be completely constant. The installation ratio of the front suspension shows to be slightly degressive at first before turning into progressive for a larger damper travel. The installation ratio of the rear suspension shows to be slightly progressive. This is presented in Figure 4.13 and Figure 4.14.

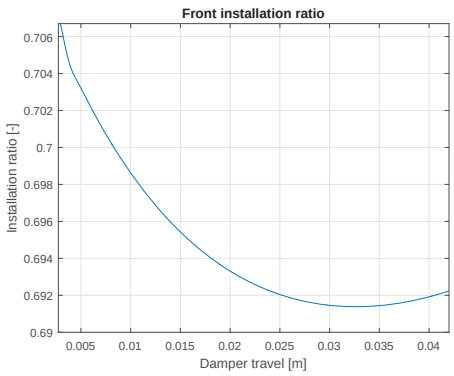

Figure 4.13: *The designed front installation ratio according to the multi-body model*

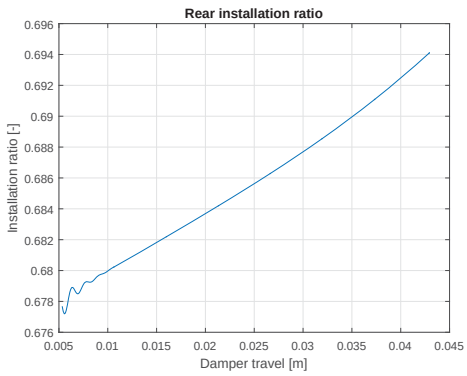

Figure 4.14: *The designed rear installation ratio according to the multi-body model*

The change of the installation ratio is only around 2 % in both cases. Therefore, it is assumed to be constant. By looking at the vertical wheel center travel against the damper compression in Figure 4.15 and 4.16, the same conclusion can be drawn, since this shows a linear graph. For this calculation a certain amount of preload to the multi-body model suspension to make it completely rebound in static position, thus having a damper travel of 0 mm. To make the suspension in the model go to being fully compressed, with a damper travel of 43 mm, a ramp is used to linearly increase the vertical force on the chassis.

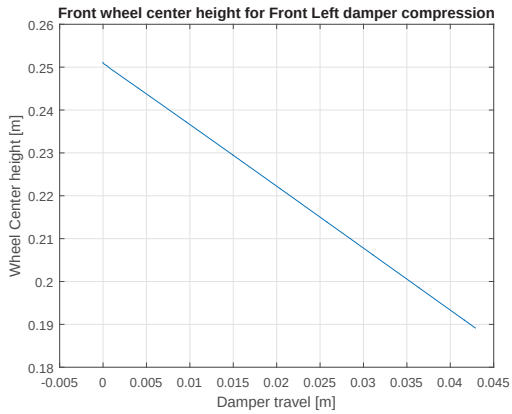

Figure 4.15: *The front wheel center height against the damper compression*

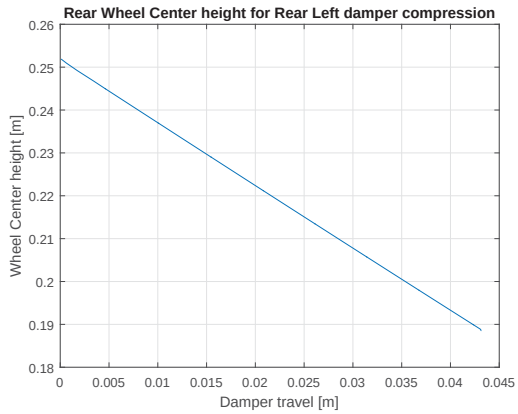

Figure 4.16: *The rear wheel center height against the damper compression*

Figure 4.17 and 4.18 show the installation ratio as a function of spring compression for both the design and the measurement results. Here, the spring travel from the measurements is compensated for the static friction, since this isn't modeled in the multi-body model. This is done by using the mean of the compression and rebound case for the spring travel.

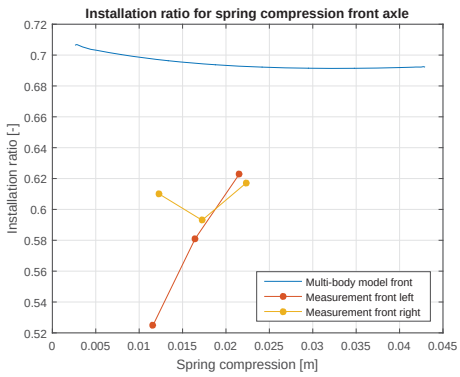

Figure 4.17: *Front suspension installation ratio from measurement results and design values*

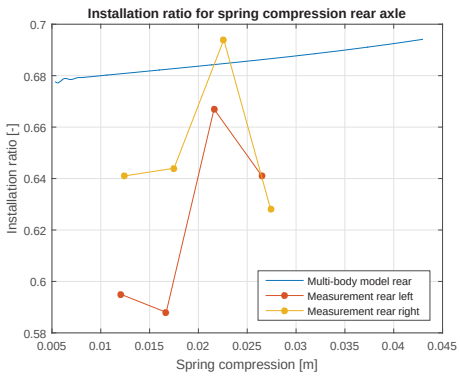

Figure 4.18: *Rear suspension installation ratio from measurement results and design values*

It is clear that the measurements to determine the installation ratio and the spring stiffness need to be improved. As mentioned, the difference between measurement results and design values for the front axle is to some extend caused by poor measurements using a tape measure. But at the rear, where this isn't the case, the differences are large as well. Furthermore, the shape of the measurement graphs are nowhere near the shape of the design value graphs. In order to improve the results, there are several possibilities. For instance, the spring length can be measured using linear potentiometers and the ride height can be measured using optical sensors, this will reduce the human error from measuring with a sliding caliper. Also, it is favorable to have more data points to see a clearer trend in the data. Furthermore, using scales with a higher resolution improves the measurement accuracy. Finally, the static friction affects the spring stiffness measurement, however this is measured and accounted for. Even after improving the measurement protocol, there may still be differences between the measured values and the design values, caused by the difference in the design and manufactured suspension. As an additional measurement, the suspension geometry can be measured on the URE11.

5 Validation using vehicle measurements

After researching the behavior of the suspension statically, research is conducted on the dynamic behavior. In this chapter, the effects of different drive types, torque set points, torque distributions and the influence of anti-effects on the suspension deflection are researched. These effects are researched by looking at vehicle test data, simulations executed with the multi-body model (MBM) and by comparing the two.

5.1 First test day

At the first vehicle test day, acceleration runs are performed, with rear wheel drive (RWD), as the front final drives were broken at the time. At this test day, the torque set point is varied to be 400, 500 and 600 Nm, for the three anti-effect settings. The measurement data showed minimal damper travel. This was caused by a high preload setting, discovered afterwards. Since the damper travel data is crucial for the comparison with the multi-body model and to look at the effects of different anti-effect settings, the gathered data from this test day is not further processed and analyzed for this research.

5.2 Second test day

At the second test day with the URE11, acceleration runs of 75 m are driven with varying drive types and torque set points. On this test day, the front- and rear wing were removed from the vehicle. Also, no control algorithms are implemented to limit the tire slip. The applicable vehicle parameters are listed in Table 2.1. The preload is completely removed from the springs. The driver of the day was Lars Hermans, who is 2 m tall and weighs 75 kg. The center of gravity height of the vehicle has been tested with several drivers seated and without a driver. During this measurement the front wing and rear wing were attached. One of the measured drivers was 1.95 m tall and weighed 73 kg. With that driver seated, the center of gravity height equals 0.30 m. The center of gravity height on the test day is therefore assumed to be 0.30 m as well. On the test day longitudinal acceleration runs with all wheel drive (AWD), with different torque set points and torque distributions are driven. Furthermore longitudinal acceleration runs with rear wheel drive (RWD) and front wheel drive (FWD), with different torque set points are driven. During every acceleration run, the driver completely floors the accelerator pedal as fast as possible to accelerate from standstill. The tire temperature is measured several times during the test day. After warm-up laps the tire temperature was around 15 $°C$. During the longitudinal acceleration runs the tire temperature was around 10 $°C$. At 10 $°C$ the tire pressure was around 0.94 bar. The atmospheric temperature was around 3.5 $°C$. For the front wheel drive runs, a torque distribution p_d of 0.05 needed to be programmed, since a flaw in the software caused a torque distribution of 0.00 to be rear wheel drive instead of front wheel drive.

5.3 tire-road friction coefficient estimation

For the comparison of the measurements with the multi-body model it is necessary to have an estimation of the tire-road friction coefficient μ during the test day. If this is the same for the model as for the test day, the vehicle in the simulation should have the same amount of traction. For this estimation the equations of Section 3.5 will be used. This results in a graph for the maximum amount of axle torque that can be applied while not surpassing the traction limit, for a front wheel drive and rear wheel drive vehicle as shown in Figure 5.1 and 5.2 respectively.

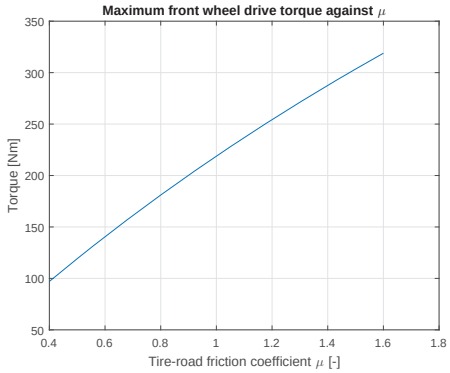

Figure 5.1: *The maximum amount of FWD axle torque for tire-road friction coefficient μ*

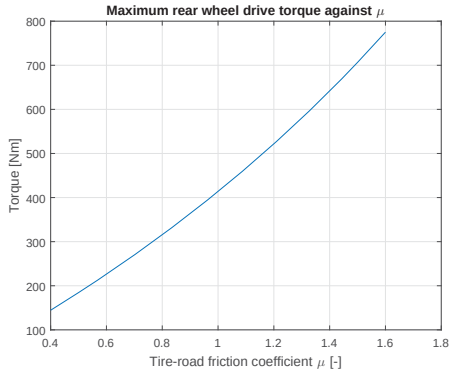

Figure 5.2: *The maximum amount of RWD axle torque for tire-road friction coefficient μ*

The maximum amount of axle torque for which there wasn't excessive wheel spin during acceleration gives the value of μ. Figure 5.3 shows 2 runs with 200 Nm maximum axle torque and 3 runs with 150 Nm. This shows that the maximum axle torque was approximately 150 Nm. This corresponds to a tire-road friction coefficient μ of 0.65 for the front wheel drive acceleration runs. Figure 5.4 shows 4 runs with 500 Nm, 2 runs with 550 Nm and 2 runs with 450 Nm maximum axle torque. This shows that the maximum axle torque was approximately 450 Nm. This corresponds to a tire-road friction coefficient μ of 1.05 for the rear wheel drive acceleration runs. With the rear wheel drive tire-road friction coefficient μ being almost twice the value of the front wheel drive, it can be concluded that this method of estimating μ is inaccurate. For the comparison between the measurements and the model, the μ of the model is set to 1.8 so it isn't a limitation.

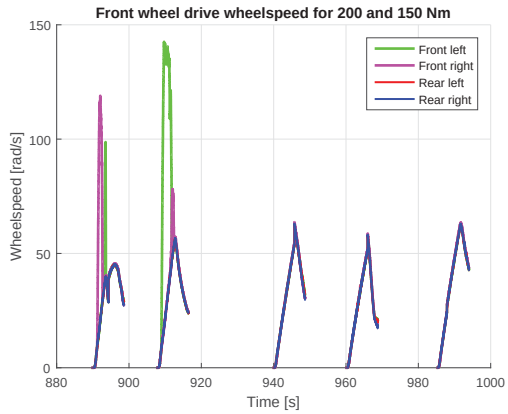

Figure 5.3: *The measured wheelspeeds for 2 runs on 200 Nm axle torque and 3 runs on 150 Nm*

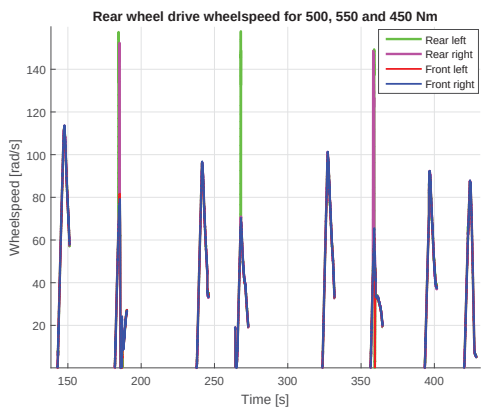

Figure 5.4: *The measured wheelspeeds for 4 runs on 500 Nm axle torque, 2 runs on 550 Nm and 2 runs on 450 Nm*

5.4 Longitudinal acceleration for different drive types

One of the benefits of having four electric motors powering the vehicle is that they can be controlled individually. Therefore, the drive type of the vehicle can easily change. To see how different drive types perform on longitudinal acceleration and to see how big the advantage of one is, measurements are conducted using front-, rear- and all wheel drive. The longitudinal acceleration runs are performed with different torque set points, to seek the traction limit for each drive type. The hypotheses is that a front wheel drive vehicle has the lowest longitudinal acceleration, since load transfer during acceleration reduces the vertical tire force on the front tires and increases on the rear tires. An all wheel drive vehicle should have the highest longitudinal acceleration, since it can utilize all the tires

to propel the vehicle. This corresponds with the maximum amount of driving torque per axle as calculated in Section 3.5.
To see if there is a difference in longitudinal acceleration between drive types, and between the multi-body model results and the measurement results, three cases are analyzed. For the results, the runs are averaged and filtered before comparing them. For the multi-body model results a 5 Hz bandwidth filter is used and for the measurement results a 2 Hz bandwidth filter. For the first case, the front wheel drive and rear wheel drive longitudinal accelerations are compared on 150 Nm. For both types, 3 runs are driven. Also, the front wheel drive acceleration is compensated for the flaw in torque distribution, needing to be 0.05, by dividing by 95 and multiplying by 100. The result of this comparison is shown in Figure 5.5. For the second case, the rear wheel drive and all wheel drive accelerations are compared on 450 Nm. For all wheel drive, 3 runs are driven and for rear wheel drive 2 runs. The result of this comparison is shown in Figure 5.6. For the third case, the front-, rear- and all wheel drive longitudinal acceleration runs are compared on their maximum longitudinal acceleration, using 150 Nm, 450 Nm and 600 Nm respectively. The result of this comparison is shown in Figure 5.7.

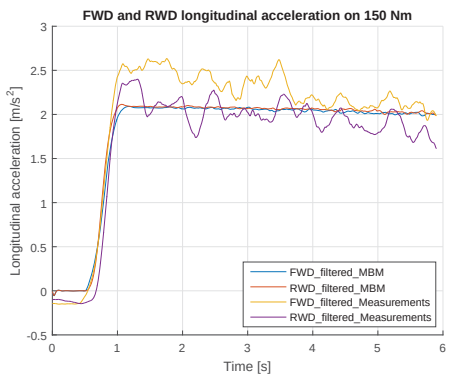

Figure 5.5: *Acceleration comparison of 3 FWD and RWD runs, model and measurement results*

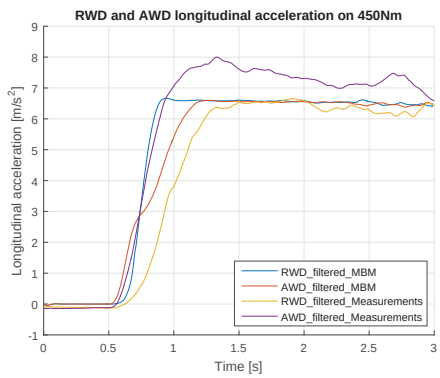

Figure 5.6: *Acceleration comparison of 3 AWD and 2 RWD runs, model and measurement results*

The results of the first two cases show that for the multi-body model, the acceleration itself doesn't depend on the drive type, but solely on the amount of torque for a certain vehicle. The difference in longitudinal acceleration for the measurement results can be caused by a difference in tire-road friction coefficient μ, resulting in a difference in the amount of tire slip and thus, longitudinal acceleration. The last case clearly shows that the all wheel drive type is capable of achieving the highest longitudinal acceleration with a maximum amount of 600 Nm torque with a torque distribution of 0.19.

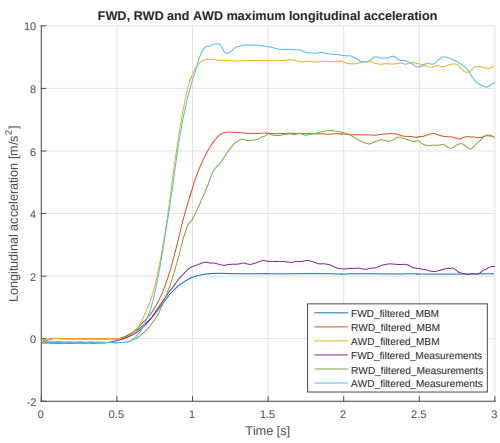

Figure 5.7: *The maximum measured acceleration for FWD, RWD and AWD, model and measurement results*

5.5 Damper travel different drive types

Besides looking at the longitudinal acceleration, it is also interesting to look at the damper travels, to see the difference between drive types and the difference between the measurements and the multi-body model. The same comparisons are made as in Section 5.4 and the data is processed in the same way. The initial value of the measurement data is corrected to overlap with the multi-body model data. Figure 5.8 and 5.9 show the damper travel comparison for front- and rear wheel drive on 150 Nm. Figure 5.10 and 5.11 show the second comparison, for rear- and all wheel drive on 450 Nm. In these graphs, 0 cm damper travel corresponds to full rebound, thus an increasing amount of damper travel corresponds to suspension compression.

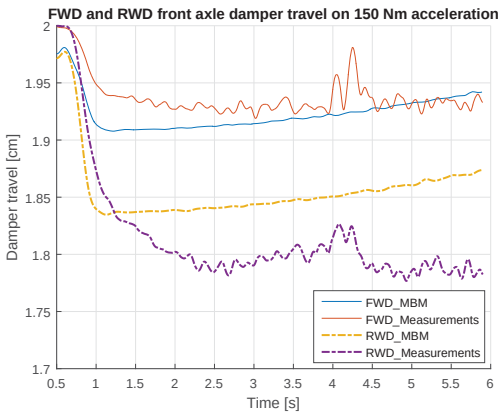

Figure 5.8: *Front axle damper travel comparison of 3 FWD and RWD runs, model and measurement results*

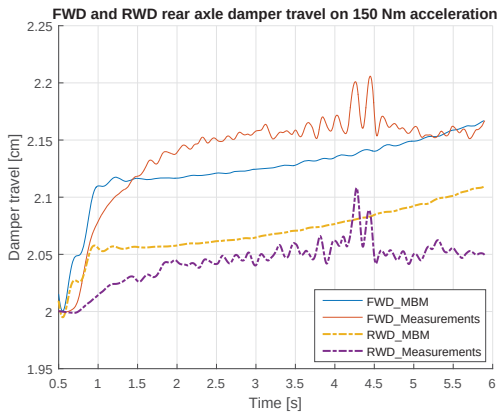

Figure 5.9: *Rear axle damper travel comparison of 3 FWD and RWD runs, model and measurement results*

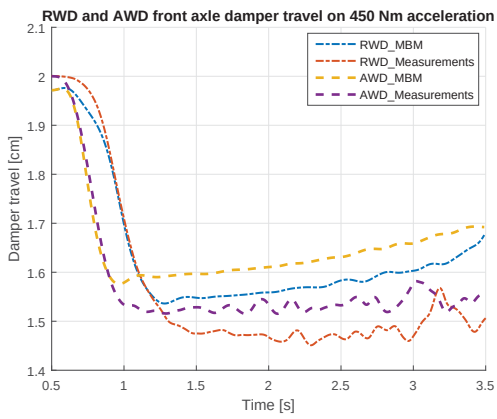

Figure 5.10: *Front axle damper travel comparison of 3 AWD and 2 RWD runs, model and measurement results*

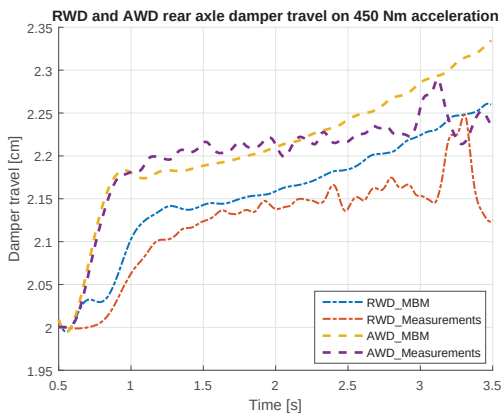

Figure 5.11: *Rear axle damper travel comparison of 3 AWD and 2 RWD runs, model and measurement results*

The anti-effect is clearly visible in Figures 5.8 and 5.9. For the front wheel drive longitudinal acceleration, there is anti-lift, which causes the front dampers to rebound (extend) less than in the rear wheel drive case. For the rear wheel drive acceleration, there is anti-squat, which causes the rear dampers to compress (squat) less than in the front wheel drive case. The deviation between the rear- and all wheel drive acceleration damper travel in the second comparison can be explained by anti-lift on the front axle and by anti-squat on the rear axle. In the all wheel drive case there is more torque on the front axle and less on the rear axle relative to the axle torque for the rear wheel drive case, as the total amount of torque is the same. This causes the front dampers in the rear wheel

drive case to rebound (lift) more and the rear dampers in the all wheel drive case to compress (squat) more.
In general, the dampers in the multi-body model compress more during longitudinal acceleration than in the measurements. The multi-body model seems to have a higher aerodynamic coefficient of lift K_L than in reality. This is illustrated by an increase in damper compression over time. As the velocity increases over time in these runs, the amount of downforce increases and with that, the amount of damper compression increases too.

The damper travels for the third case, the maximum acceleration case are shown in Figure 5.12 and 5.13.

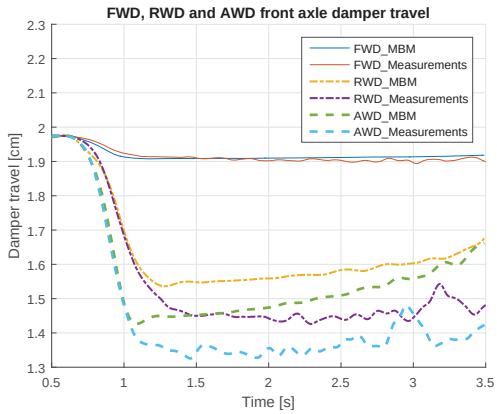

Figure 5.12: *Front axle damper travel under maximum acceleration for FWD, RWD and AWD, multi-body model and measurement results*

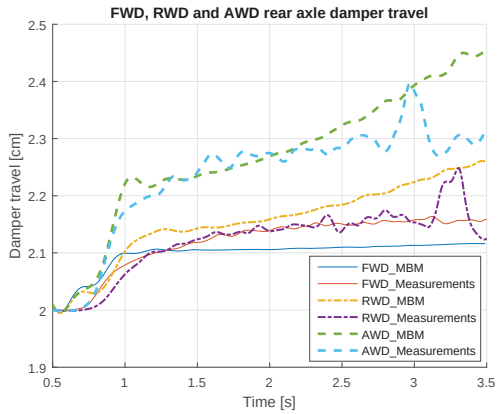

Figure 5.13: *Rear axle damper travel under maximum acceleration for FWD, RWD and AWD, multi-bode model and measurement results*

To see what the differences between the multi-body model results and the measurement results is, the difference in damper travel is calculated in between 1.5 and 2 seconds, in which the damper travel is assumed to be constant. The results are shown in Table 5.1.

Table 5.1: *The deviation between multi-body model and measurement results based on the average damper travel in the domain of 1.5 to 2 seconds.*

Drive type	**MBM** [cm]	**Measurements** [cm]	**Deviation** [%]
FWD Front axle	1.909	1.907	-0.1
FWD Rear axle	2.106	2.132	1.2
RWD Front axle	1.553	1.450	-6.6
RWD Rear axle	2.149	2.135	-0.7
AWD Front axle	1.462	1.346	-7.9
AWD Rear axle	2.249	2.265	0.7

Consistently, the deviation is smallest on the driven axle. Furthermore, the deviation increases for an increase in longitudinal acceleration. This can also be seen in graphs such as Figure 5.8.

5.6 Anti-effects

The damper travel graphs of Section 5.5 show the effect of anti-lift and anti-squat on the damper travel to some extend. To research the anti-effect further, several longitudinal acceleration runs are driven with varying support angles on the rear axle θ_R. As mentioned in 3.4.1, the support angle θ can be varied by adjusting the rear top front (RTF) suspension point. As this is only done on the rear axle, the acceleration runs are driven using rear wheel drive. Thus, the rear/front torque distribution, p_d equals 1. The aerodynamic coefficient of lift K_L in the multi-body model is set to 0,

to have no influence of aerodynamics in this analysis. The longitudinal acceleration runs are driven with a 400 Nm torque set point. The results are visualized in Figure 5.14. Again, the numerical deviations are calculated. A time interval of 2 to 3 seconds is considered to have constant damper travel. The results are shown in Table 5.2. Here BOT represents the situation in which the upper wishbone of the rear suspension is tilted to the lowest position, as shown in Figure A.1. In this setting the support angle θ_R is 10.52 degree. MID represents the middle setting, with a support angle θ_R of 6.19 degree and TOP represents the case for which the wishbone is tilted to the highest pick-up point, with a support angle of θ_R of -1.80 degree.

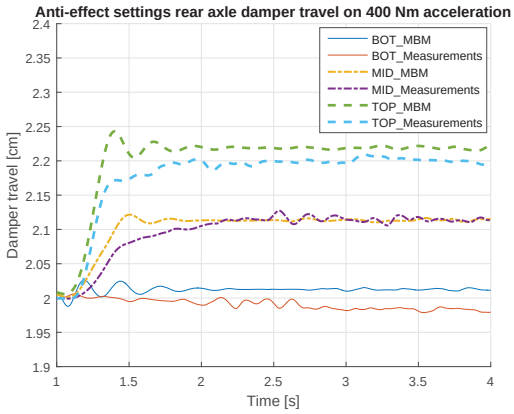

Figure 5.14: *Rear axle damper travel comparison for rear wheel drive longitudinal acceleration runs with varying support angles*

Table 5.2: *The deviation between multi-body model and measurement results based on the average damper travel in the domain of 2 to 3 seconds.*

Drive type	**MBM** $[cm]$	**Measurements** $[cm]$	**Deviation** %
BOT Rear axle	2.013	1.991	-1.1
MID Rear axle	2.113	2.115	-0.1
TOP Rear axle	2.219	2.197	-1.0

The increase in damper travel over time is not present in this analysis. This means that the change in K_L is effective. It is interesting to see that the deviation between the multi-body model and measurement results is larger for the bottom and top setting. The middle setting is the standard setting for which the suspension is originally designed. Generally, the multi-body model corresponds to the measurements wuite well.

When looking only at the measurement results, an analysis on the influence of the support angle itself on the amount of damper travel can be made. The results are presented in Table 5.3. Here, MID-BOT shows the deviation in damper travel between using the middle setting and the bottom setting with average travel 1 being the damper travel in the middle setting and average travel 2 being the damper travel in the bottom setting.

Table 5.3: *The difference between support angle settings*

1-2	**Average travel 1** $[cm]$	**Average travel 2** $[cm]$	**Deviation** %
MID-BOT	2.115	1.991	-6.2
MID-TOP	2.115	2.197	3.7
BOT-TOP	1.991	2.197	10.3

These results show that, on the rear axle, an increase of the support angle θ_R, decreases the damper travel and a decrease in the support angle θ_R increases the amount of damper travel for a certain longitudinal acceleration.

For the damper travel on the free rolling axle, the deviation between the multi-body model results and measurement results is larger than on the driven axle. This observation is supported by the results, for this analysis, on the front axle in Figure 5.15.

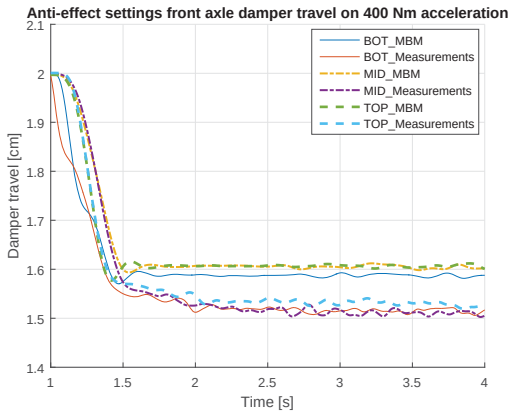

Figure 5.15: *Front axle damper travel comparison for rear wheel drive longitudinal acceleration runs with varying support angles*

6 The multi-body model improvements

During the comparison of the measurement results with the multi-body model, several issue's needed to be solved, in order to make the model work appropriately and more accurate. In this chapter these problems and solutions are discussed briefly.

6.1 Chassis center of gravity

The multi-body model works with four centers of gravity. The front- and rear unsprung masses $m_{unsprung}$ have a center of gravity $h_{CoG,unsprung}$ and the front- and rear sprung masses m_{sprung} have a center of gravity $h_{CoG,sprung}$. In the model the sprung masses m_{sprung} used a center of gravity height which corresponds with the center of gravity height of the entire vehicle $h_{CoG,tot}$, with total vehicle mass m_{tot}. This is changed to Equation 6.1.

$$h_{CoG,sprung} = \frac{m_{tot} * h_{CoG,tot} - m_{unsprung} * h_{CoG,unsprung}}{m_{sprung}} \tag{6.1}$$

6.2 Damper travel

In the static position, the suspension in the multi-body model corresponds with the suspension designed in Siemens NX, using the coordinates of the suspension attachment points. In this position, the dampers are at the middle of their stroke, however in the multi-body model this corresponds to zero damper travel. The damper travel is changed to be zero at full rebound by subtracting half of the stroke from the calculated position.
For the validation of the installation ratio, a simulation needs to be done in which the suspension travels from full rebound to full compression, so it travels over the entire damper stroke. Therefore, preload is added to rebound the suspension. However, the anti-roll system in the multi-body model limited the dampers to always have a minimum compression of 17 mm. This issue is solved by removing the anti-roll system. Since this thesis is about longitudinal acceleration, this isn't a problem for the simulations done with the multi-body model, but it still needs to be solved for future use.

6.3 Aerodynamics

When looking at the damper travels during longitudinal acceleration without a front wing and rear wing installed on the vehicle, it can be concluded that the coefficient of lift K_L of the body aerodynamics in the multi-body model does not correspond to reality. For the analysis of the anti-effects, the K_L of the body aerodynamics has been changed from 0.9 to 0. This removes the increase of damper travel with velocity and causes the damper travel over time to correspond better to the measurements. Further research on the K_L of the body aerodynamics, without the use of the front and rear wing, is recommended.

7 Conclusions and Recommendations

In this thesis, the suspension is analyzed for static and dynamic conditions, analyzing the installation ratio, spring and damper travels, several anti-effects and the static friction.

The static measurements are conducted twice with an increasing accuracy. The second measurement method still needs to be improved as the measurement results had larger deviations than expected, also in comparison with the design.
The measured static friction in the suspension is around 2 mm on the front axle spring travel, corresponding to 27.5 N and 3 mm on the rear axle spring travel, corresponding to 41.2 N.

The dynamic measurements for the longitudinal acceleration using different drive types and torque set points is conducted twice with increasing accuracy. This resulted in reliable results. The results of the multi-body model correspond fairly well to the measurement results, for both the longitudinal acceleration and the damper travel. The damper travels on the (major) driven axle corresponded to the model with a deviation smaller than 1 %, whereas the deviation on the free rolling or minor driven axle ranged from 1.2 to 7.9 %. It is uncertain what causes the results for the free rolling or minor driven axle measurements to have a larger deviation to the multi-body model results than the measurement results for the driven axle. The body aerodynamic lift coefficient K_L was too high. This is changed to zero to better represent reality. The measurements of the anti-effects resulted in reliable data. The results of the multi-body model correspond to the measurement results within 1.1 % and show to have a relatively large influence on the damper travel in general.

As only a small part of the suspension is validated in this thesis, additional research is valuable for the understanding of the suspension and for the improvement of the multi-body model on the following subjects.

static validation

The static validation measurements can be improved, primarily by using sensors to measure the spring travel and ride height deviation and by increasing the axle mass in smaller steps, to get more measurement points. Also, the use of scales with a higher resolution improves the measurement accuracy. Furthermore, the suspension geometry on the URE11 must be measured, as this can be one of the causes for deviations in the comparison between the measurement results and the design. To extend this research, the static friction in isolated components, such as the dampers can be measured, as well as validating the method of adjusting preload on the suspension. Furthermore, the combination of roll stiffness and degrees of vehicle roll is an interesting subject to research, which has an influence on the cornering behavior of the vehicle.

dynamic validation

Besides knowing that all wheel drive can obtain the highest longitudinal accelerations compared to front- and rear wheel drive, the torque distribution between the front and rear axle has an influence on the longitudinal acceleration of the vehicle. Therefore, it is important to improve the estimation of the tire-road friction coefficient μ. For the validation of damper travel in the multi-body model, it is uncertain what causes the deviation between the measurement and multi-body model results to be larger for the free rolling or minor driven axle. For the anti-effects, further research can be conducted on the influence on the longitudinal acceleration. In the dynamic measurements, the influence of static friction on the longitudinal acceleration of the vehicle can also be researched.

multi-body model

Several improvements are made to the multi-body model during this thesis, but the modelling of the anti-roll system can be improved. This needs to be resolved in order to conduct research on the cornering behavior of the vehicle. Furthermore, what causes the deviations between the measurement results and the design needs to be researched.

References

[1] Dr. Ir. I.J.M. Besselink (2015) *Introduction Vehicle Dynamics and Powertrains - 4AUB0*, Dynamics & Control Technology (D&C), Eindhoven University of Technology, Eindhoven.

A URE 11

In this appendix several pictures are shown of the URE11. These are pictures to explain components of the URE11 and how the static tests are performed.

A.1 Anti-effects rear suspension

Figure A.1 shows part of the rear right suspension with on the right the rear top front (RTF) bracket with which the support angle can be altered. In this picture the wishbone is placed at the bottom setting, which will result in a support angle of 10.52 degrees.

Figure A.1: *The rear right suspension of the URE11*

A.2 Static test

Figure A.2 shows the vehicle resting on leveled scales, with one block of 20 kg added on the rear axle. This is shown for the front axle in Figure A.3. Figure A.4 shows the measurement of the spring length, using a sliding caliper. The measurement for the change of the ride height for the rear axle is shown in Figure A.5, for the front axle it is shown in Figure A.6. For this measurement, the distance between the chassis and a beam, placed on the leveled scales is measured on three points on the chassis.

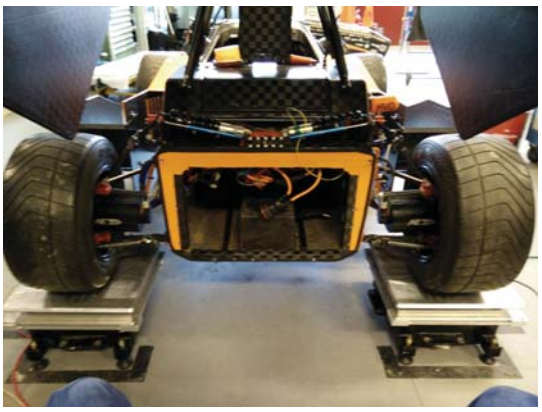

Figure A.2: *Adding mass to the rear axle.*

Figure A.3: *Adding mass to the front axle.*

Figure A.4: *Measuring the spring length.*

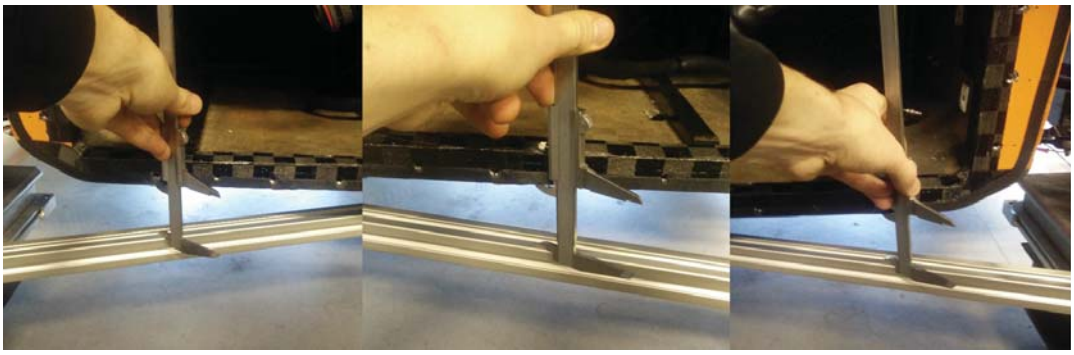

Figure A.5: *Measuring the ride height on the rear.*

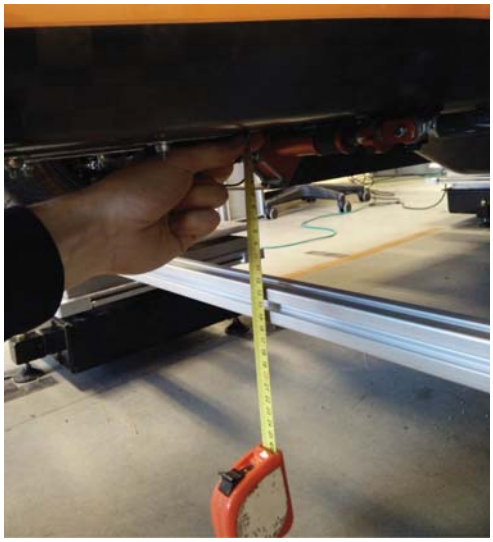

Figure A.6: *Measuring the ride height on the front axle using a tape measure.*

B Static measurement results

In this appendix, the measurement data of the static measurements is presented. The measured parameters are the mass, measured using the scales, the damper travel and the ride height.

B.1 Measurement 1

Table B.1: *First measurement on the front suspension*

Mass [kg]		**Damper travel [mm]**		**Ride height [mm]**			
FL	FR	FR	FR	Left	Middle	Right	Average
37.5	29	80.5	84	125	125	125	125
46.5	37.5	78	81	122	122	122	122
56	46	75.5	78.5	115	115	115	115
64.5	55	72.9	76.6	111	111	111	111

Table B.2: *First measurement on the rear suspension*

Mass [kg]		**Damper travel [mm]**		**Ride height [mm]**			
RL	RR	RL	RR	Left	Middle	Right	Average
33.5	41.5	73.7	72	56.5	56.5	56.5	56.5
43.5	51	72	70.4	53.5	53.5	53.5	53.5
53	60.5	71	69.5	50.7	50.7	50.7	50.7
63.5	69	69.3	67.2	47.3	47.2	47.2	47.23
73.5	77.5	67.8	65.6	43.7	43.5	43.5	43.57

B.2 Measurement 2

Table B.3: *Second measurement on the front suspension*

Mass [kg]		**Damper travel [mm] bump**		**Damper travel [mm] rebound**		**Ride height [mm] bump**	**Ride height [mm] rebound**
FL	FR	FL	FR	FL	FR	Average	Average
35	36	112.6	112.2	113.5	114	117.67	120
43.5	45	107.4	106.8	109.4	108.6	108.33	111.5
52.5	54	102.4	101.8	104.7	103.7	100	103
61.5	63	97.3	96.8	99.6	98.6	91.5	95

Table B.4: *Second measurement on the rear suspension*

Mass [kg]		**Damper travel [mm] bump**		**Damper travel [mm] rebound**		**Ride height [mm] bump**	**Ride height [mm] rebound**
RL	RR	RL	RR	RL	RR	Average	Average
35.5	34.5	112	112	114.1	114.2	59.27	62.2
45.5	43	106.7	106.2	109.2	109	50.37	53.8
55.5	52	102	101	104.6	104	41.9	46.3
65.5	61	96.8	95.8	100	99	34.67	38.7
75	70	91.8	90.8	95.2	94.4	26.53	31.4